

EMISSION FROM MAGNETIZED ACCRETION DISKS AROUND YOUNG STARS

C. TAPIA¹ AND S. LIZANO¹

¹Instituto de Radioastronomía y Astrofísica, UNAM, Apartado Postal 3-72, 58089 Morelia, Michoacán, México

ABSTRACT

We calculate the emission of protoplanetary disks threaded by a poloidal magnetic field and irradiated by the central star. The radial structure of these disks was studied by Shu and collaborators and the vertical structure was studied by Lizano and collaborators. We consider disks around low mass protostars, T Tauri stars, and FU Ori stars with different mass-to-flux ratios λ_{sys} . We calculate the spectral energy distribution and the antenna temperature profiles at 1 mm and 7 mm convolved with the ALMA and VLA beams. We find that disks with weaker magnetization (high values of λ_{sys}) emit more than disks with stronger magnetization (low values of λ_{sys}). This happens because the former are denser, hotter and have larger aspect ratios, receiving more irradiation from the central star. The level of magnetization also affects the optical depth at millimeter wavelengths, being larger for disks with high λ_{sys} . In general, disks around low mass protostars and T Tauri stars are optically thin at 7 mm while disks around FU Ori are optically thick. A qualitative comparison of the emission of these magnetized disks, including heating by an external envelope, with the observed millimeter antenna temperature profiles of HL Tau indicates that large cm grains are required to increase the optical depth and reproduce the observed 7 mm emission at large radii.

Keywords: accretion disks – ISM:magnetic fields – protoplanetary disks – radiative transfer – stars: formation – stars: protostars

1. INTRODUCTION

During the process of gravitational collapse and protoplanetary disk formation, one expects that the magnetic field from the parent dense core will be dragged into the disk. Nevertheless, it has been found that, if the field remains frozen in the gas during the collapse, it would produce the so-called catastrophic magnetic breaking and prevent the formation of a rotationally supported disk (RSD). To allow the formation of RSDs several processes have been proposed like magnetic field dissipation at high densities or the reduction of the torques by a misalignment between the magnetic field direction and the rotation axis (e.g., see review by [Lizano & Galli 2015](#)). The magnetic field left over from these processes will permeate the protoplanetary disk allowing for the operation of the magneto rotational instability (MRI) which provides a natural mechanism for the disk viscosity ([Balbus & Hawley 1998](#)).

Linearly polarized millimeter emission at disk scales has been observed toward a few protostars like IRAS 16293-2422B ([Rao et al. 2014](#)), HL Tau ([Stephens et al. 2014](#)), L1527 ([Segura-Cox et al. 2015](#)), and NGC 1333 IRAS 4A1 ([Cox et al. 2015](#)). If the polarized light is produced by emission from elongated dust grains aligned with respect to the magnetic field lines, the polarization vectors rotated by 90 degrees give the direction of the magnetic field lines (e.g., see review by [Lazarian 2007](#)). In these sources the magnetic field seems to have an important toroidal component, expected in young sources with substantial infalling envelopes. Recently, [Kataoka et al. \(2015\)](#) pointed out that polarization due to dust self-scattering by large grains in disks can be very important at millimeter wavelengths, when the maximum grain size is $a_{\text{max}} \sim \lambda/2\pi$, where λ is the observing wavelength. In this case, the scattering mass opacity due to large grains can be as large as the absorption opacity (see their Figure 1). To produce polarized light, an asymmetry in the distribution of the light source is also required. The contributions of both elongated dust emission and self-scattering depend on the disk structure. In particular, [Yang et al. \(2016\)](#) calculated the contribution of both dust emission and scattering as a function of the disk inclination to explain the observed polarization in NGC 1333 IRAS 4A1. [Yang et al. 2016](#) and [Kataoka et al. 2016](#) also argued that the millimeter polarization in HL Tau can be explained by dust

scattering. With the advent of ALMA many more observations of disks will soon be available and it will be possible to disentangle the contribution of both mechanisms to obtain the morphology and structure of the disk magnetic field.

Shu et al. (2007) (hereafter S07) studied models of the radial structure of accretion disks threaded by a poloidal magnetic field, dragged from the parent dense core during the phase of gravitational collapse. The magnetized disk models of S07 consider a thin cold accretion disk with negligible mass in force balance in the radial direction. The disk has sub-Keplerian rotation due to the magnetic tension of the poloidal field such that the rotation rate is $\Omega = f\Omega_K$, where the sub-Keplerian factor is $f < 1$ and $\Omega_K = (GM_*/\varpi^3)^{1/2}$, where G is the gravitational constant, M_* is the stellar mass, and ϖ is the radial coordinate (see their eq. [18]). The disk evolves due to the viscosity ν that transfers angular momentum outward and allows the matter in the inner regions to accrete, and the resistivity η that allows the matter to cross field lines. Steady state models require that the dragging of field lines by the accretion flow is balanced by the outward field diffusion. As found by Lubow et al. (1994), this implies a small ratio of the resistivity to the viscosity (the inverse of the Prandtl number), $\eta/\nu \sim A$, where A is the disk aspect ratio. The disks models are characterized by a mass-to-flux ratio $\lambda_{\text{sys}} = (M_* + M_d)2\pi G^{1/2}/\Phi$, where M_d is the disk mass and Φ is the magnetic flux threading the disk. The disk models assume a power-law disk aspect ratio $A(\varpi) \propto \varpi^n$ and a viscosity ν given by their eq. (3). In these models, all the disk radial variables are power-laws (see their eqs. [63]-[69], for the case $n = 1/4$).

Lizano et al. (2016) (hereafter L16) calculated the vertical structure of these magnetized disks, heated by viscous and resistive dissipation and by the radiation from the central star. They discussed disks around YSOs with strong magnetization ($\lambda_{\text{sys}} = 4$) and disks with weaker magnetization ($\lambda_{\text{sys}} = 12$). The strongly magnetized disks are highly compressed by the magnetic pressure. In the case of the T Tauri disk, this large compression could be in conflict with the disk scale heights inferred from observations, suggesting that a significant amount of magnetic field has to be dissipated during the process of disk formation. Their Table 2 shows the values of the aspect ratio $A_{\lambda_{\text{sys}}}$, and the surface density $\Sigma_{\lambda_{\text{sys}}}$, for disk models with different mass-to-flux ratios.

In this paper we discuss the emission of the magnetized accretion disks studied by L16, including the spectral energy distribution (SED) and the averaged antenna temperature at 1 mm and 7 mm convolved with the ALMA and VLA beams, respectively. In §2, we describe the method of solution. In §3, we present the main results. In §4 we compare the emission of the models with the observed mm antenna temperature profiles of the source HL Tau. In §5 we discuss processes not included in the present study. Finally, in §6 we present the conclusions.

2. METHOD OF SOLUTION

We consider the emission of magnetized disks around young stars subject to both viscous and resistive heating and irradiated by the central star, using the vertical structure models discussed by L16. We study disks around low mass protostars (LMP), T Tauri stars, and FU Ori stars with different levels of magnetization measured by the mass-to-flux ratio λ_{sys} . For the different star plus disk systems we obtain the SED and the averaged antenna temperature profiles at 1 mm and 7 mm.

Given the vertical structure of the disk and an inclination angle θ between the disk rotation axis and the line of sight (l.o.s.), we solve the radiative transfer equation through the disk along rays parallel to the l.o.s. (coordinate Z), in a grid of points covering the area of the disk projected on the plane of the sky. Because the dust albedo at millimeter wavelengths is high for large grains as discussed in §1, the scattered light emissivity is included. We integrate along each ray the monochromatic intensity I_ν ($\text{erg s}^{-1} \text{cm}^{-2} \text{Hz}^{-1} \text{str}^{-1}$) and the monochromatic optical depth τ_ν given by

$$\frac{dI_\nu}{d\tau_\nu} = -I_\nu + S_\nu, \quad \text{and} \quad \frac{d\tau_\nu}{dZ} = -\chi_\nu \rho, \quad (1)$$

where S_ν is the source function, ρ is the disk local density, and the total opacity is $\chi_\nu = \kappa_\nu + \sigma_\nu$, where κ_ν is the mass absorption coefficient, and σ_ν is the scattering coefficient. The source function for an isotropically scattering medium is given by $S_\nu = (1 - \omega_\nu)B_\nu + \omega_\nu J_\nu$, where the albedo is $\omega_\nu = \sigma_\nu/\chi_\nu$, B_ν is the Planck function at the local temperature, and J_ν is the mean intensity (Mihalas 1978). Following D’Alessio et al. (2001), J_ν is approximated by the mean intensity of a vertically isothermal slab found by Miyake & Nakagawa (1993), given by their eq. (28). The effect of including scattering is to increase the optical depth, and, for a given total disk opacity, the flux from an optically thick region is reduced with respect to a purely absorbing medium, as shown in their Figure 22.

We assume a dust composition given by a mixture of silicates, organics, and water ice with a mass fractional abundance with respect to the gas $\zeta_{\text{sil}} = 3.4 \times 10^{-3}$, $\zeta_{\text{org}} = 4.1 \times 10^{-3}$, and $\zeta_{\text{ice}} = 5.6 \times 10^{-3}$, with bulk densities $\rho_{\text{sil}} = 3.3 \text{ g cm}^{-3}$, $\rho_{\text{org}} = 1.5 \text{ g cm}^{-3}$, and $\rho_{\text{ice}} = 0.92 \text{ g cm}^{-3}$ (Pollack et al. 1994). The dust particles have a power-law size distribution, $n(a) \propto a^p$, with an exponent $p = 3.5$, a minimum grain size $a_{\text{min}} = 0.005 \mu\text{m}$, and maximum grain

size $a_{\max} = 1$ mm. We assume that the dust and gas are well mixed. The solid lines in the upper panels of Figure 1 of D’Alessio et al. (2001) show the mass absorption coefficient κ_ν as a function of wavelength for $a_{\max} = 1$ mm, for a temperature $T = 100$ K and $T = 300$ K. At 300 K the NIR opacity features disappear because the water ice has sublimated. The upper right panel of their Figure 2 shows that the contribution of troilite to κ_ν , not included in our calculation, is small for $\lambda < 1$ mm. We use the code of D’Alessio et al. (2001) that includes gas opacity at $T > 1,400$ K. The opacity sources are free-free and bound-free transitions from neutrals and ions of H, He, H₂, Si, Mg, C, molecular bands from CO, TiO, OH and H₂O, and scattering by H, He, H₂ and electrons (Calvet et al. 1991).

The parameters of the LMP, the T Tauri, and the FU Ori star plus disk systems are shown in Table 1. The first column corresponds to the Young Stellar Object (YSO), the second column shows the disk mass accretion rate \dot{M}_d , the third column shows the disk mass M_d , the fourth column shows the radius of the central star R_* , and the fifth column shows the total central luminosity L_c , including the accretion luminosity, that irradiates the disk surface.

3. RESULTS

We calculate the structure and emission of disks around YSOs with different levels of magnetization, measured by the mass-to-flux ratio λ_{sys} . We consider strongly magnetized disks with a low value of $\lambda_{\text{sys}} = 4$ and disks with a weaker magnetization with high values of $\lambda_{\text{sys}} = 12$ and 24. Following S07, we assumed a viscosity coefficient $D = 1$ for the LMP and the FU Ori disks. For the T Tauri disks we assume two values of the viscosity coefficient $D = 10^{-2.5}$ and 0.01. As discussed by S07, a small value of D for the T Tauri disks represents inefficient disk accretion due to dead zones near the disk mid-plane. The properties of the disk models are summarized in Table 2¹. The first column corresponds to the YSO and each value of the mass-to-flux ratio $\lambda_{\text{sys}} = 4, 12$ and 24; the second column shows the sub-Keplerian factor f ; the third column shows the disk aspect ratio $A_{\lambda_{\text{sys}}}$ at 100 AU; the fourth column shows the column density $\Sigma_{\lambda_{\text{sys}}}$ at 100 AU; the fifth column shows the vertical component of the magnetic field $B_{\lambda_{\text{sys}}}$ at 100 AU; the sixth column shows the disk radius R_d ; and the seventh column shows the ratio of the thermal to magnetic pressure at 1 AU, the plasma β_1 ². The radial profiles of the aspect ratio, surface density, and vertical component of the magnetic field are given by $A(\varpi) = A_{\lambda_{\text{sys}}}(\varpi/100 \text{ AU})^{1/4}$, $\Sigma(\varpi) = \Sigma_{\lambda_{\text{sys}}}(\varpi/100 \text{ AU})^{-3/4}$, and $B_z(\varpi) = B_{\lambda_{\text{sys}}}(\varpi/100 \text{ AU})^{-11/8}$. The radial component of the magnetic field at the disk surface is $B_\varpi^+ = 1.742B_z$ (see Table 1 of S07). The plasma β varies slowly with radius $\beta(\varpi) = \beta_1(\varpi/1 \text{ AU})^{1/4}$ for disks with high λ_{sys} where the departure from Keplerian rotation is small, and is constant for disks with low λ_{sys} (see eqs. (47) and (48) of S07).

Figure 1 shows the radial and vertical temperature profiles of the LMP disks for different values of λ_{sys} . The upper panels show the radial temperature profiles of the mass weighted temperature $\langle T \rangle = 2 \int_0^{\Sigma(\varpi)/2} T d\Sigma / \Sigma(\varpi)$; the mid-plane temperature T_c , and $T_{z_{90}}$, the temperature at the location of the mass surface z_{90} ³. These panels also show the irradiation temperature T_{irr} at the surface z_{irr} , where the irradiation from the central star is absorbed. The lower panels show the vertical temperature profiles at different radii. The star symbol corresponds to the location of the irradiation surface z_{irr} , and the diamond symbol corresponds to the location of the mass surface z_{90} . The vertical temperature profiles show a temperature inversion close to the disk surface due to the external heating of the disk surface (see e.g., Figure 4 of D’Alessio et al. 1998). The mid-plane temperature increases with λ_{sys} due to the increase of the surface density: for the same disk mass M_d , disks with weaker magnetization (high λ_{sys}) are more compact than disks with stronger magnetization (low λ_{sys}).

The upper panels of Figure 2 show the different surfaces of the LMP disks: the disk surface z_∞ , the irradiation surface z_{irr} , and the mass surface z_{90} . The lower panels show the SEDs of the star plus disk systems at different inclination angles θ . For a large inclination angle $\theta = 80^\circ$, the emission from the star is occulted by the disk. A silicate feature at $\sim 10\mu\text{m}$ can be observed in the $\lambda_{\text{sys}} = 4$ SED at $\theta = 80^\circ$.

Figure 3 shows the radial and vertical temperature profiles of T Tauri disks with viscosity coefficient $D = 10^{-2.5}$ for different values of λ_{sys} . Figure 4 shows the different disk surfaces and the SEDs at different inclination angles. Because the disk radii are small (see Table 2), we decided to explore also the T Tauri model with a viscosity coefficient $D = 0.01$. This coefficient determines the magnitude of the viscosity (see eq. [42] of S07). The radial structure changes with D as shown in eqs. (63) - (69) of S07. For $D = 0.01$ the surface density is smaller and, for the same disk mass, R_d is larger than the models with $D = 10^{-2.5}$ (see Table 2). Figures 5 and 6 show the temperature profiles,

¹ These values have been slightly modified compared to those shown in Table 2 of L16 due to a new iteration scheme of the vertical structure models.

² The disk properties are obtained solving the equations of the radial structure (S07) and the vertical structure (L16). In particular, the aspect ratio $A_{\lambda_{\text{sys}}}$ is not a free parameter. It is obtained from the thermal balance where one takes into account viscous and resistive heating and irradiation by the central star. Once $A_{\lambda_{\text{sys}}}$ is calculated, one can obtain the corresponding disk surface density and magnetic field according to eqs. (63) and (64) of S07. This is an iterative procedure that continues until $A_{\lambda_{\text{sys}}}$ converges and one obtains the full vertical structure.

³ This surface contains 90% of the disk mass (see discussion in §5 of L16).

disk surfaces, and SEDs of these models. Because the disks are geometrically thin, the emission from the central star always contributes to the SED. The effect of magnetic compression is evident in the disks with $\lambda_{\text{sys}} = 4$, where the height of the z_{∞} , z_{irr} , and z_{90} surfaces are lower than than the models with higher values of λ_{sys} .

Figure 7 shows the radial and vertical temperature profiles of FU Ori disks with different λ_{sys} . Figure 8 shows the different surfaces and SEDs. The disks sizes are very small (3 - 16 AU) and correspond to the region in the disks where the FU Ori outburst is expected to occur. The magnetic compression of the $\lambda_{\text{sys}} = 4$ disk is evident in the top panels of Figure 8. In this case, the disk is geometrically thin and the emission from the star contributes to the SED even at large inclination angles. In contrast, in the disks with $\lambda_{\text{sys}} = 12$ and 24, the star is occulted by the disk for large inclination angles and does not appear in the SED.

Radial profiles of the averaged antenna temperature T_B and optical depth τ_{λ} are shown in Figures 9 - 11. The antenna temperature is given by $T_B \equiv \lambda^2 I_{\nu} / 2k_B$, where k_B is the Boltzmann constant. The antenna temperature is averaged over ellipsoidal annuli with an eccentricity given by $e = \sin \theta$. The disks shown have $\theta = 60^\circ$. The 1 mm and 7 mm profiles are shown in the upper and lower panels, respectively. The dashed lines show the profiles convolved with the ALMA beam at 1 mm, $\theta_{\text{ALMA}} = 0.034''$, and the VLA beam at 7 mm, $\theta_{7\text{mm}} = 0.043''$. In general, the convolved antenna temperature profiles decrease with respect to the model profiles, but are within the sensitivity levels of these facilities. The dotted lines correspond to the optical depth, shown in the left axis in each panel⁴.

The averaged antenna temperature profiles of the LMP and T Tauri disks show that disks with weaker magnetization (high λ_{sys}) emit more than disks with stronger magnetization (low λ_{sys}): they have larger values of the antenna temperature T_B at a given radius. Table 3 gives the ratio of the fluxes at 1 mm and 7 mm with respect to the fluxes of the $\lambda_{\text{sys}} = 4$ disk. At 7 mm the flux ratios are larger than 1. Disks with high λ_{sys} emit more because they are denser and hotter than disks with low λ_{sys} . For the same reason, the T Tauri disk with a viscosity coefficient $D = 10^{-2.5}$ has larger values of T_B at each wavelength than the T Tauri disk with $D = 0.01$. At 1 mm, the flux ratios are smaller than 1 for the LMP and the FU Ori disks. This happens because the disks are optically thick and the $\lambda_{\text{sys}} = 4$ disks have larger sizes than disks with high λ_{sys} . The optical depth profiles in these figures also show that disks with high λ_{sys} are more optically thick than the disks with low λ_{sys} because they are denser. Also, the $\lambda_{\text{sys}} = 4$ and 12 disks around LMP and T Tauri stars are optically thin at 7 mm, except in the $\sim 1 - 2$ AU central region. In contrast, the FU Ori disks are optically thick because they are very small and dense; thus, the antenna temperature reaches large values, of the order of the kinetic temperature, $T_B \sim T \sim 1000$ K. Also, the 7 mm profile of the $\lambda_{\text{sys}} = 4$ FU Ori disk shows a sharp decrease in the emission at ~ 3 AU. This happens because there is a contribution from gas opacity for $T > 1,400$ K (see §2). These large temperatures occur only in the mid-plane of the inner 2 AU, nevertheless, this region is projected in the plane of the sky up to ~ 3 AU due to the disk inclination angle.

The LMP and the T Tauri disks are optically thick at 1mm and, because the disk are truncated at R_d , at an inclination angle of 60° the emission from the hot disk mid-plane at outer edge of the hemisphere closest to the observer produces an increase of the averaged antenna temperature at external disk radii. This effect is observed in the 1 mm profiles of the $\lambda_{\text{sys}} = 24$ disks in the upper right panels of Figures 9 - 11. It also produces a ‘‘bump’’ around $\sim 3 \mu\text{m}$ in the FU Ori SED for $\theta = 60^\circ$ and 80° . Nevertheless, this is an artifact of the assumed disk truncation at R_d . Instead, the surface density of viscously evolving disks is expected to have an exponential decay, $\Sigma = \Sigma_d (\varpi/R_d)^{-\gamma} \exp(-(\varpi/R_d)^{2-\gamma})$ (Lynden-Bell & Pringle 1974). For the magnetized models discussed in these work $\gamma = 3/4$. To obtain more realistic temperature profiles at the external radii, one needs to include this exponential region beyond R_d which would attenuate the bright disk edge. Assuming $\rho(\varpi) \sim \Sigma/(A(\varpi)\varpi)$, one obtains a radial optical depth $\tau_{\nu} = \int \kappa_{\nu} \rho d\varpi = I_0 \kappa_{\nu} (\Sigma_{\text{sys}}/A_{\text{sys}}) (R_d/100\text{AU})^{-2}$, where $I_0 = \int_1^{1+R_{\text{ext}}/R_d} u^{-2} \exp(-u^{5/4}) du \sim 0.12$ for $R_{\text{ext}} \sim 2R_d$. Assuming $\kappa_{1\text{mm}} \sim 0.01$, the LMP and T Tauri disks with $\lambda_{\text{sys}} = 24$, have an optical depth $\tau_{1\text{mm}} > 1$. Thus, an external exponential region can attenuate the bright rim of the truncated disks. Nevertheless, the modification of the radial models of S07 to include this surface density exponential decay is out of the scope of this paper.

The surface density and temperature structure of the magnetized disk models discussed here are the result of a mechanical and thermal equilibrium. As example, in the next section we apply these models to an observed disk to obtain information of its physical properties.

⁴ The integration of the optical depth is stopped at 25 for numerical convenience.

4. APPLICATION TO HL TAU

In this section we model the emission of LMP disks with the characteristics of the well known Class I source HL Tau whose spectacular structure was recently observed with ALMA (Alma partnership 2014). This source is located in the Taurus cloud at a distance of 140 pc. The disk shows multiple rings whose origin and physical conditions have motivated many recent observational and theoretical studies (e.g., Jin et al. 2016; Okuzumi et al. 2016; Ruge et al. 2016; Takahashi & Inutsuka 2016; Yen et al. 2016). Figure (3) of Carrasco-González et al. (2016) shows the antenna temperature profiles of HL Tau at 0.87 mm, 1.3 mm, 2.9 mm, and 7 mm, obtained with ALMA and VLA. We make a qualitative comparison of the emission of the magnetized disk models with these temperature profiles to obtain general properties of the HL Tau disk, instead of modelling the detailed ring structure as done recently, for example, by Pinte et al. (2016) with a parametrized disk structure.

D’Alessio et al. (1997) showed that irradiation by the HL Tau envelope is needed to heat the disk and raise its temperature in the outer regions to reproduce the observed fluxes at mm wavelengths. Thus, to compare with the observed mm profiles, we include a simple envelope heating: we assume that the disk is irradiated by a thermal bath with a temperature T_e such that, at the disk surface, the mean intensity due to the envelope irradiation is $J_e = \sqrt{3}\sigma T_e^4/(4\pi)$. Then, J_e is added to the B.C. in eq. (45) of L16, and the envelope flux $(4\pi/\sqrt{3})J_e e^{(-\tau_d)}$ is also added to the reprocessed flux in their eq. (41), where τ_d is the opacity normal to the disk mid-plane.

HL Tau has observational estimates of disk mass, radius, accretion rate, and luminosity which are a little different from the reference LMP model discussed in Section 3. For example, the disk mass of HL Tau is 50 % higher and the disk accretion rate is 50% lower than the LMP model. The disk radius is obtained from eq. (65) of S07, with A_{sys} calculated self-consistently from the vertical structure modelling (L16). We find that the $\lambda_{\text{sys}} = 12$ models are too large, with $R_d = 466$ AU. For this reason, we consider magnetized disk models with $\lambda_{\text{sys}} = 24$ which have $R_d \sim 100$ AU, as observed in this source (Kwon et al. 2011).

Table 4 shows the parameters chosen for the HL Tau disk: the mass accretion rate \dot{M}_d , the disk mass M_d , the luminosity of the central source L_c that includes the stellar and the accretion luminosities, the inclination angle θ , the mass-to-flux ratio λ_{sys} , and the sub-Keplerian factor f . We assume a central star with mass $M_* = 1 M_\odot$, radius $R_* = 2.2 R_\odot$ and a temperature $T_* = 4,000$ K. We discuss 6 LMP disk models (Model I - VI) that have different envelope temperatures $T_e = 0, 50, 100$ K and different values of the maximum grain size $a_{\text{max}} = 1$ mm, 1 cm. For these models, Table 5 shows the aspect ratio $A_{\lambda_{\text{sys}}}$, the mass surface density $\Sigma_{\lambda_{\text{sys}}}$ at 100 AU, the vertical component of the magnetic field B_{sys} at 100 AU, the disk radius R_d , and the plasma β_1 at 1 AU.

The upper panels of Figure 12 show the convolved antenna temperature profiles T_B at 0.87 mm, 1.3 mm, 2.9 mm, and 7 mm. The lower panels show the corresponding convolved optical depth profiles τ_λ . The left panels correspond to Model I (dotted lines), Model II (solid lines), and Model III (dashed lines) which have a dust distribution with $a_{\text{max}} = 1$ mm. The emission is optically thick from 0.87 mm to 2.9 mm, thus, Model I without envelope heating is too cold to reproduce the ALMA profiles. On the other hand, Model III, which has a substantial envelope heating ($T_e = 100$ K), overestimates the antenna temperatures at these wavelengths. The observed 7 mm profile cannot be reproduced by Models I - III. Because the emission at 7 mm is optically thin, the 7 mm profiles have very low temperatures at 100 AU. In order to increase the opacity, we decided to explore models with a dust distribution with $a_{\text{max}} = 1$ cm. The right panels correspond to Model IV (dotted lines), Model V (solid lines), and Model VI (dashed lines), which have a dust distribution with $a_{\text{max}} = 1$ cm. The effect of the large grains is to increase the optical depth at 7 mm. As before, the temperature profiles of Model IV (with no envelope heating) are too low at all wavelengths, while the temperature profiles of Model VI ($T_e = 100$ K) are too high for 0.87 mm to 2.9 mm.

The observed temperature profiles of Carrasco-González et al. (2016) are best reproduced by Model V which has a moderate envelope heating ($T_e = 50$ K). This model also reproduces the observed 7 mm VLA profile. This happens because its opacity increased by a factor of 10 with respect to the models with $a_{\text{max}} = 1$ mm. Note that the 7mm opacity reported by Carrasco-González et al. (2016) is a factor of ~ 15 lower than the opacity of Model V. Nevertheless, Carrasco-González et al. (2016) assumed a dust temperature profile and, from the simple equation of radiative transfer $T_B = T_d(1 - e^{-\tau_\nu})$, solved for the optical depth τ_ν (see the first paragraph in Section 3.1 of their paper). Since Model V reproduces the level of observed emission at 7 mm, if one applies the same procedure, one would obtain optical depths similar to their values. Instead, what is plotted in the lower panels of Figure 12 is the physical optical depth profiles of the models convolved with the ALMA and VLA beams.

From this qualitative study we find that it is difficult to reproduce the observed emission at 7 mm of the HL Tau disk at large radii just including the envelope heating. We conclude that one possibility is that the HL Tau disk has large grains at the external radii which can increase the optical depth. Then, with both envelope heating and large

grains, Model V can produce the observed level of 7 mm emission at the external radii.

5. PHYSICAL PROCESSES NOT INCLUDED IN THIS STUDY

In the models discussed in this work we have not considered several processes. These include dust growth, settling and radial migration which are expected to occur in protoplanetary disks (for a review see [Williams & Cieza 2011](#)). Also, we do not include physical processes like the formation of vortices or spiral arms that have been observed in several sources (e.g., [van der Marel et al. 2016](#); [Pérez et al. 2016](#)).

Grain growth can be taken into account by considering different values of a_{\max} . Dust settling can be included by considering an atmospheric layer with small grains and a mid-plane layer with larger grains such that the dust mass missing from the atmospheric layer is incorporated into the mid-plane layer ([D'Alessio et al. 2006](#)). The degree of settling is measured by the ratio of the dust to gas mass ratio of the small grains in the atmospheric layer to the total dust to gas mass ratio, $\epsilon = \zeta_{\text{small}}/\zeta_T \leq 1$. The settling scale height is usually a free parameter although it could be established by the balance of gravitational sedimentation and turbulent diffusion (e.g., [Dubrulle et al. 1995](#)), or from observations as in the case of [Pinte et al. \(2016\)](#) who inferred a very thin dust disk in the case of HL Tau. Dust radial drift has been studied by many authors (e.g., [Takeuchi & Lin 2002](#); [Brauer et al. 2008](#); [Birnstiel et al. 2010](#)). Their models show that this process should occur in very short timescales, in conflict with the observations of disks that infer mm and cm dust grains in the external regions of disks. Nevertheless, recent high resolution mm observations have found a radial gradient in dust sizes in several sources (e.g., [Pérez et al. 2015](#); [Tazzari et al. 2016](#)). Then, to include the effect of the dust radial drift one can assume a radial variation of a_{\max} together with a variation of ζ_T . The inclusion of all these processes will be the subject of a future study.

It will be interesting to model other T Tauri and FU Ori sources when high spatial resolution ALMA and VLA data will be available, that can provide information about the disk temperature and optical depth, as in the case of HL Tau. In particular, to study older disks, processes like settling and radial migration need to be included in our models.

Finally, the relevant range of values of λ_{sys} in protoplanetary disks will eventually come from observations or from models and numerical simulations of disk formation.

6. CONCLUSIONS

We calculate the emission of magnetized accretion disks irradiated by the central star using the vertical structure models of L16. We consider disks with different levels of magnetization, measured by the mass-to-flux ratio λ_{sys} . We include the SED and the averaged antenna temperature profiles at 1 mm and 7 mm, convolved with highest angular resolution beams of ALMA and VLA.

We find that disks with weaker magnetization (high values of the mass-to-flux ratio λ_{sys}) emit more than disks with stronger magnetization (low values of λ_{sys}). This happens because the former disks are denser and have larger aspect ratios. Thus, they receive more irradiation from the central star and are hotter than the more strongly magnetized disks. The optical depth at millimeter wavelengths also varies with the level of magnetization because disks with high λ_{sys} are denser than disks with low λ_{sys} . Disks around LMP and T Tauri stars are optically thick at 1mm and are optically thin at 7 mm. Instead, the FU Ori disks are always optically thick.

We compare the emission of magnetized disk models with observed mm antenna temperature profiles of the disk of HL Tau. We find that models with a dust distribution with a maximum grain size $a_{\max} = 1$ mm do not reproduce the observed 7 mm profile, even including the heating due to the envelope irradiation. Because the emission is optically thin, the 7 mm antenna temperature drops to very low values at large radii. One possibility is the HL Tau disk has large grains, with $a_{\max} = 1$ cm, that increase the dust opacity. Then, together with the envelope heating, the disk can reach the observed 7 mm emission at the external radii.

In the near future, one expects that high angular resolution observations of magnetic fields from disks around young stars will be obtained with the ALMA and VLA interferometers. It will be very useful to compare these observations with the structure and emission of the magnetized disks models discussed in this work. This comparison can help constrain the level of magnetization in protoplanetary disks, measured by their mass-to-flux ratio, to understand their formation and evolution.

CT and SL acknowledge support by CONACyT 153522 and UNAM-PAPIIT 105815. They also acknowledge valuable comments and suggestions from an anonymous referee which helped improved this manuscript.

REFERENCES

- ALMA Partnership, Brogan, C. L., Pérez, L. M., et al. 2015, *ApJL*, 808, L3
- Balbus, S. A., & Hawley, J. F. 1998, *Reviews of Modern Physics*, 70, 1

- Birnsteil, T., Dullemond, C. P., & Brauer, F. 2010, *A&A*, 513, A79
- Brauer, F., Dullemond, C. P., & Henning, T. 2008, *A&A*, 480, 859
- Calvet, N., Patino, A., Magris, G. C., & D'Alessio, P. 1991, *ApJ*, 380, 617
- Cox, E. G., Harris, R. J., Looney, L. W., et al. 2015, *ApJL*, 814, L28
- Carrasco-González, C., Henning, T., Chandler, C. J., et al. 2016, *ApJL*, 821, L16
- D'Alessio, P., Calvet, N., & Hartmann, L. 1997, *ApJ*, 474, 397
- D'Alessio, P., Cantö, J., Calvet, N., & Lizano, S. 1998, *ApJ*, 500, 411
- D'Alessio, P., Calvet, N., & Hartmann, L. 2001, *ApJ*, 553, 321
- D'Alessio, P., Calvet, N., Hartmann, L., Franco-Hernández, R., & Servín, H. 2006, *ApJ*, 638, 314
- Dubrulle, B., Morfill, G., & Sterzik, M. 1995, *Icarus*, 114, 237
- Jin, S., Li, S., Isella, A., Li, H., & Ji, J. 2016, *ApJ*, 818, 76
- Kataoka, A., Muto, T., Momose, M., et al. 2015, *ApJ*, 809, 78
- Kataoka, A., Muto, T., Momose, M., Tsukagoshi, T., & Dullemond, C. P. 2016, *ApJ*, 820, 54
- Kwon, W., Looney, L. W., & Mundy, L. G. 2011, *ApJ*, 741, 3
- Lazarian, A. 2007, *JQSRT*, 106, 225
- Lizano, S., & Galli, D. 2015, *Magnetic Fields in Diffuse Media*, 407, 459
- Lizano, S., Tapia, C., Boehler, Y., & D'Alessio, P. 2016, *ApJ*, 817, 35 (L16)
- Lubow, S. H., Papaloizou, J. C. B., & Pringle, J. E. 1994, *MNRAS*, 267, 235
- Lynden-Bell, D., & Pringle, J. E. 1974, *MNRAS*, 168, 603
- Miyake, K., & Nakagawa, Y. 1993, *Icarus*, 106, 20
- Mihalas, D. 1978, San Francisco, W. H. Freeman and Co., 1978. 650 p.,
- Okuzumi, S., Momose, M., Sirono, S.-i., Kobayashi, H., & Tanaka, H. 2016, *ApJ*, 821, 82
- Pérez, L. M., Chandler, C. J., Isella, A., et al. 2015, *ApJ*, 813, 41
- Pérez, L. M., Carpenter, J. M., Andrews, S. M., et al. 2016, *Science*, 353, 1519
- Pinte, C., Dent, W. R. F., Ménard, F., et al. 2016, *ApJ*, 816, 25
- Pollack, J. B., Hollenbach, D., Beckwith, S., et al. 1994, *ApJ*, 421, 615
- Rao, R., Girart, J. M., Lai, S.-P., & Marrone, D. P. 2014, *ApJL*, 780, L6
- Ruge, J. P., Flock, M., Wolf, S., et al. 2016, *A&A*, 590, A17
- Segura-Cox, D. M., Looney, L. W., Stephens, I. W., et al. 2015, *ApJL*, 798, L2
- Shu, F. H., Galli, D., Lizano, S., Glassgold, A. E., & Diamond, P. H. 2007, *ApJ*, 665, 535
- Stephens, I. W., Looney, L. W., Kwon, W., et al. 2014, *Nature*, 514, 597
- Takahashi, S. Z., & Inutsuka, S.-i. 2016, *AJ*, 152, 184
- Takeuchi, T., & Lin, D. N. C. 2002, *ApJ*, 581, 1344
- Tazzari, M., Testi, L., Ercolano, B., et al. 2016, *A&A*, 588, A53
- Williams, J. P., & Cieza, L. A. 2011, *ARA&A*, 49, 67
- van der Marel, N., Cazzoletti, P., Pinilla, P., & Garufi, A. 2016, *ApJ*, 832, 178
- Yang, H., Li, Z.-Y., Looney, L., & Stephens, I. 2016, *MNRAS*, 456, 2794
- Yang, H., Li, Z.-Y., Looney, L. W., et al. 2016, *MNRAS*, 460, 4109
- Yen, H.-W., Liu, H. B., Gu, P.-G., et al. 2016, *ApJL*, 820, L25

Table 1. YSOs parameters

YSO	\dot{M}_d ($M_\odot \text{yr}^{-1}$)	M_d (M_\odot)	R_* (R_\odot)	L_c (L_\odot)
LMP	2×10^{-6}	0.20	3	7.1
T Tauri	1×10^{-8}	0.03	2	0.93
FU Ori	2×10^{-4}	0.02	7	230

Table 2. Models with different mass-to-flux ratios λ_{sys}

YSO	f	$A_{\lambda_{\text{sys}}}$	$\Sigma_{\lambda_{\text{sys}}}$ (g/cm ²)	$B_{\lambda_{\text{sys}}}$ mG	R_d (AU)	β_1
LMP						
$\lambda_{\text{sys}} = 4$	0.9565	0.156	5.30	6.93	457	4.26
$\lambda_{\text{sys}} = 12$	0.9953	0.284	27.4	5.26	124	28.3
$\lambda_{\text{sys}} = 24$	0.9988	0.372	84.1	4.60	50.1	109
T Tauri ($D = 10^{-2.5}$)						
$\lambda_{\text{sys}} = 4$	0.6579	0.0123	11.0	25.8	56.0	2.92
$\lambda_{\text{sys}} = 12$	0.9679	0.102	17.6	10.9	38.2	3.85
$\lambda_{\text{sys}} = 24$	0.9921	0.193	38.2	8.01	20.6	10.0
T Tauri ($D = 0.01$)						
$\lambda_{\text{sys}} = 4$	0.6579	0.0101	4.25	16.0	120	2.81
$\lambda_{\text{sys}} = 12$	0.9679	0.090	6.33	6.53	86.9	3.70
$\lambda_{\text{sys}} = 24$	0.9921	0.163	14.2	4.89	45.5	9.12
FU Ori						
$\lambda_{\text{sys}} = 4$	0.3865	0.101	33.3	55.0	16.7	2.96
$\lambda_{\text{sys}} = 12$	0.9516	0.502	148	38.7	5.61	4.89
$\lambda_{\text{sys}} = 24$	0.9881	0.581	533	36.7	2.56	14.5

NOTE—The radial profiles of the aspect ratio, surface density, and vertical component of the magnetic field are given by $A(\varpi) = A_{\lambda_{\text{sys}}}(\varpi/100 \text{ AU})^{1/4}$, $\Sigma(\varpi) = \Sigma_{\lambda_{\text{sys}}}(\varpi/100 \text{ AU})^{-3/4}$, and $B_z(\varpi) = B_{\lambda_{\text{sys}}}(\varpi/100 \text{ AU})^{-11/8}$.

Table 3. Flux ratios

YSO	$F_{1\text{mm}}^{12}/F_{1\text{mm}}^4$	$F_{1\text{mm}}^{24}/F_{1\text{mm}}^4$	$F_{7\text{mm}}^{12}/F_{7\text{mm}}^4$	$F_{7\text{mm}}^{24}/F_{7\text{mm}}^4$
LMP	0.90	0.58	3.01	5.49
T Tauri ($D = 10^{-2.5}$)	1.62	1.05	1.58	2.49
T Tauri ($D = 0.01$)	2.23	1.89	1.91	3.19
FU Ori	0.61	0.39	1.95	1.37

NOTE—

LMP disk: $F_{1\text{mm}}^4 = 3.94 \times 10^{-1}$ Jy ; $F_{7\text{mm}}^4 = 2.11 \times 10^{-4}$ Jy .
T Tauri disk ($D = 10^{-2.5}$): $F_{1\text{mm}}^4 = 1.30 \times 10^{-2}$ Jy ; $F_{7\text{mm}}^4 = 3.54 \times 10^{-5}$ Jy .
T Tauri disk ($D = 0.01$): $F_{1\text{mm}}^4 = 1.68 \times 10^{-2}$; $F_{7\text{mm}}^4 = 1.74 \times 10^{-5}$ Jy .
Fu Ori disk: $F_{1\text{mm}}^4 = 1.75 \times 10^{-1}$ Jy ; $F_{7\text{mm}}^4 = 1.16 \times 10^{-3}$ Jy .

Table 4. HL Tau parameters

\dot{M}_d^a	M_d^b	L_c	θ^c	λ_{sys}	f
($M_{\odot}\text{yr}^{-1}$)	(M_{\odot})	(L_{\odot})	(deg)		
1×10^{-6}	0.3	8.6	47	24	0.9984

NOTE—Values taken from: (a) [D’Alessio et al. \(1997\)](#); (b) [Carrasco-González et al. \(2016\)](#); (c) [ALMA Partnership et al. \(2015\)](#) .

Table 5. HL Tau models

Model	a_{max}	T_e	$A_{\lambda_{\text{sys}}}$	$\Sigma_{\lambda_{\text{sys}}}$	$B_{\lambda_{\text{sys}}}$	R_d	β_1
		K		(g/cm^2)	mG	(AU)	
I	1 mm	0	0.215	38.6	5.09	129	63.4
II	1 mm	50	0.237	35.0	4.85	140	61.1
III	1 mm	100	0.268	30.9	4.56	154	59.4
IV	1 cm	0	0.195	42.5	5.35	119	54.1
V	1 cm	50	0.225	36.8	4.98	134	53.4
VI	1 cm	100	0.251	33.0	4.71	146	52.5

NOTE—The radial profiles of the aspect ratio, surface density, and vertical component of the magnetic field are given by $A(\varpi) = A_{\lambda_{\text{sys}}}(\varpi/100 \text{ AU})^{1/4}$, $\Sigma(\varpi) = \Sigma_{\lambda_{\text{sys}}}(\varpi/100 \text{ AU})^{-3/4}$, and $B_z(\varpi) = B_{\lambda_{\text{sys}}}(\varpi/100 \text{ AU})^{-11/8}$.

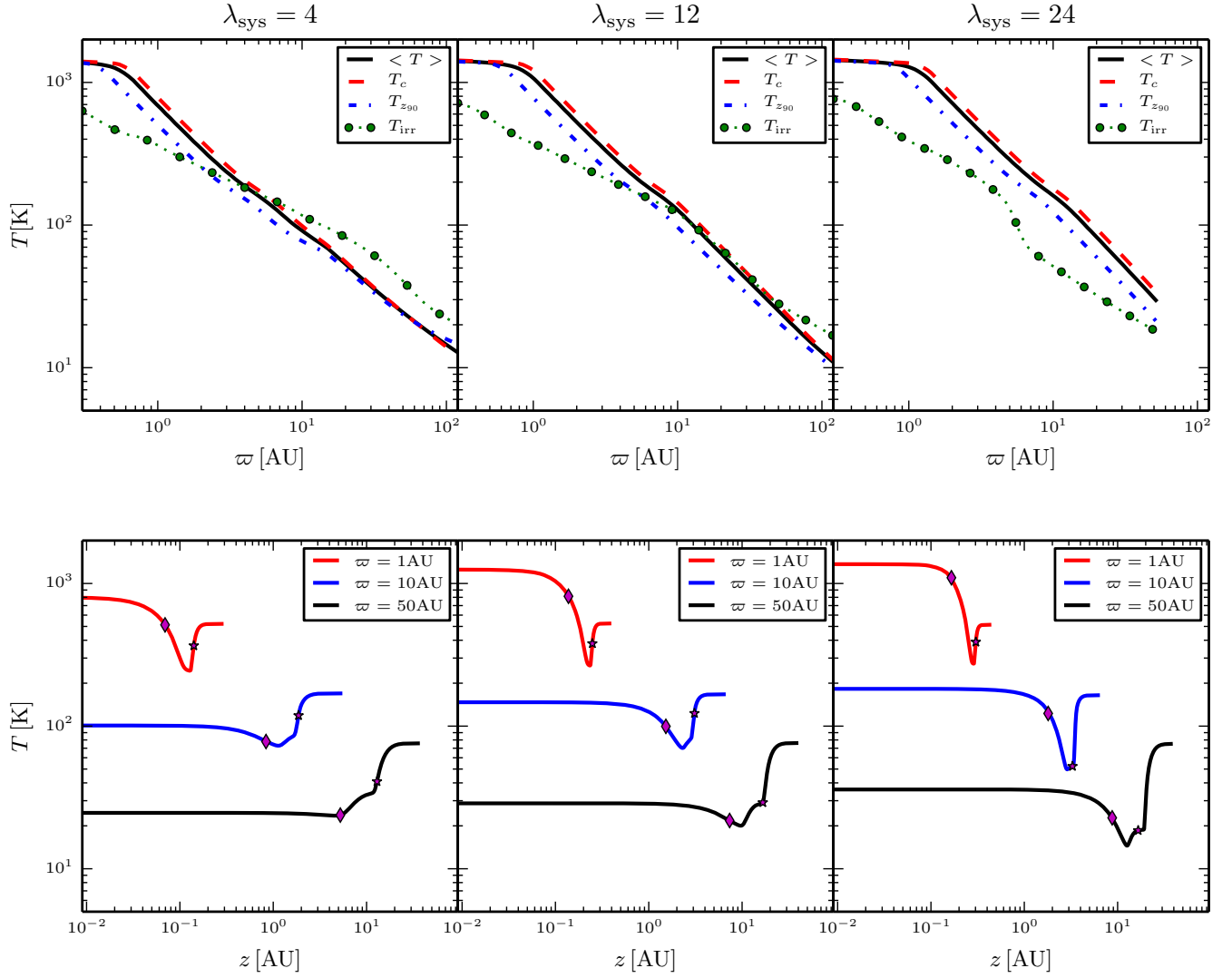


Figure 1. LMP disk models with different mass-to-flux ratios, $\lambda_{\text{sys}} = 4, 12, 24$, that label each column. The upper panels show the radial temperature profiles of the disks: the solid black lines correspond to the mass weighted temperature $\langle T \rangle$; the red dashed lines show the mid-plane temperature T_c ; the blue dot-dashed lines show the temperature of mass surface z_{90} ; the green dot lines show the temperature at the irradiation surface z_{irr} . The lower panels show vertical temperature structure at the radii indicated in the upper right boxes. The star symbol corresponds to the location of the irradiation surface z_{irr} and the diamond symbol corresponds to the location of the mass surface z_{90} .

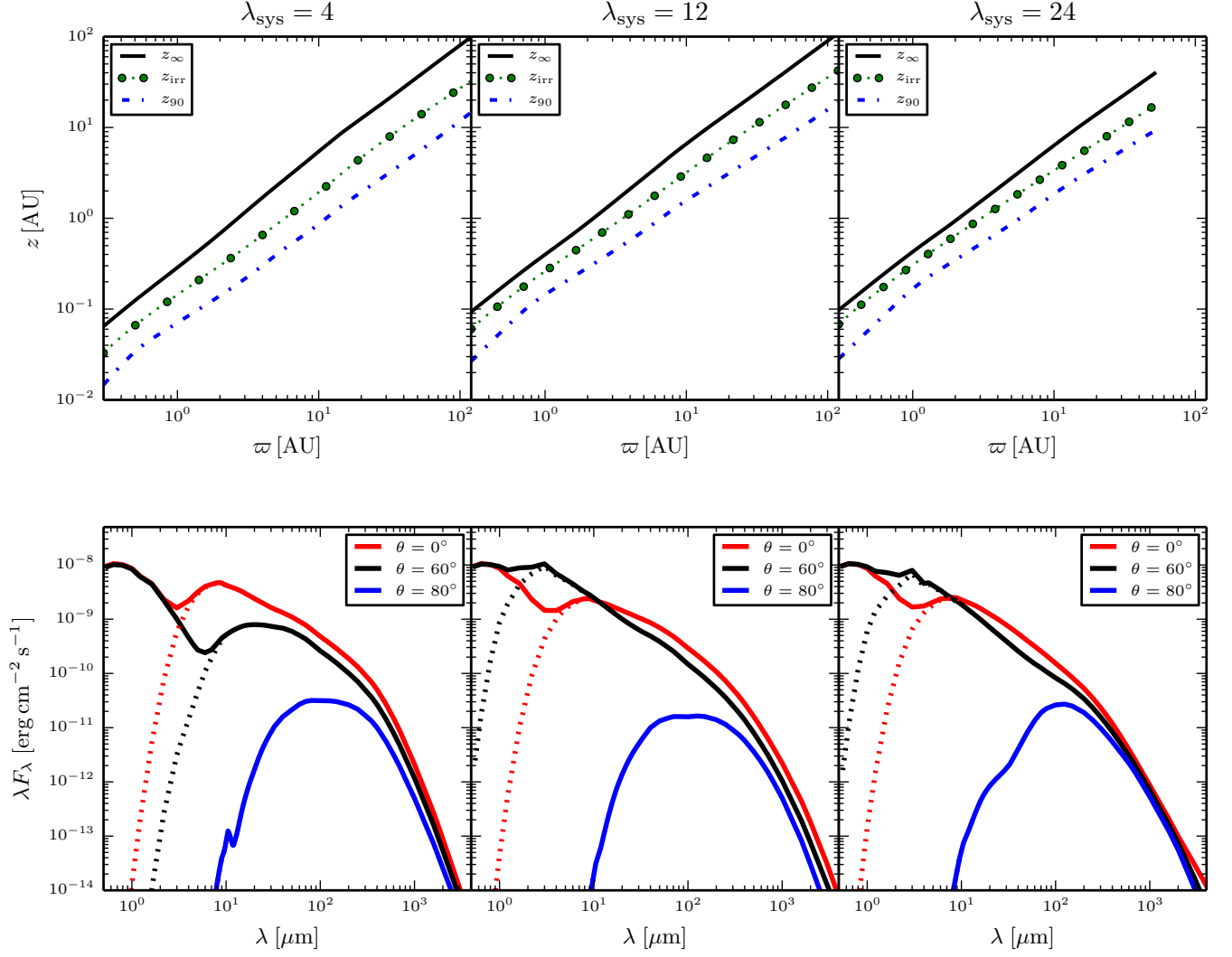


Figure 2. LMP disk models with different mass-to-flux ratios, $\lambda_{\text{sys}} = 4, 12, 24$, that label each column. The upper panels show the the different surfaces: the black solid lines show the surface of the disk z_{∞} ; the green dot lines show the irradiation surface z_{irr} ; the blue dot-dashed lines show the disk mass surface z_{90} . The lower panels show the spectral energy distribution (SED) of the star plus disk system at different inclination angles θ between the disk rotation axis and the l.o.s: $\theta = 0^\circ, 60^\circ$, and 80° (red, black and blue lines, respectively). The dotted lines show the disk contribution.

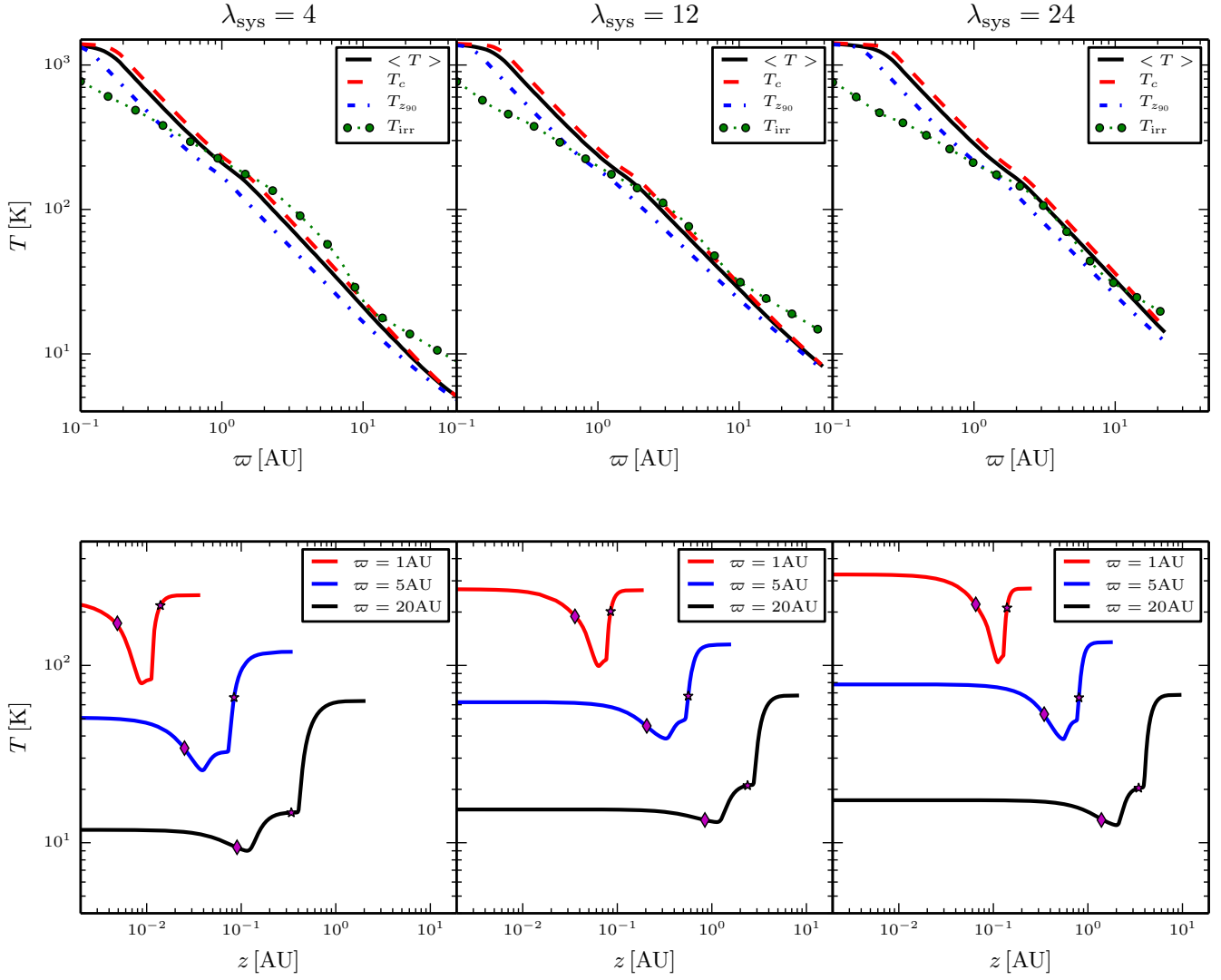


Figure 3. T Tauri disk models with viscosity coefficient $D = 10^{-2.5}$ and different mass-to-flux ratios, $\lambda_{\text{sys}} = 4, 12, 24$, that label each column. The upper panels show the radial temperature profiles of the disks. The lower panels show vertical temperature structure at the radii indicated in the upper right boxes. Same description as Figure 1.

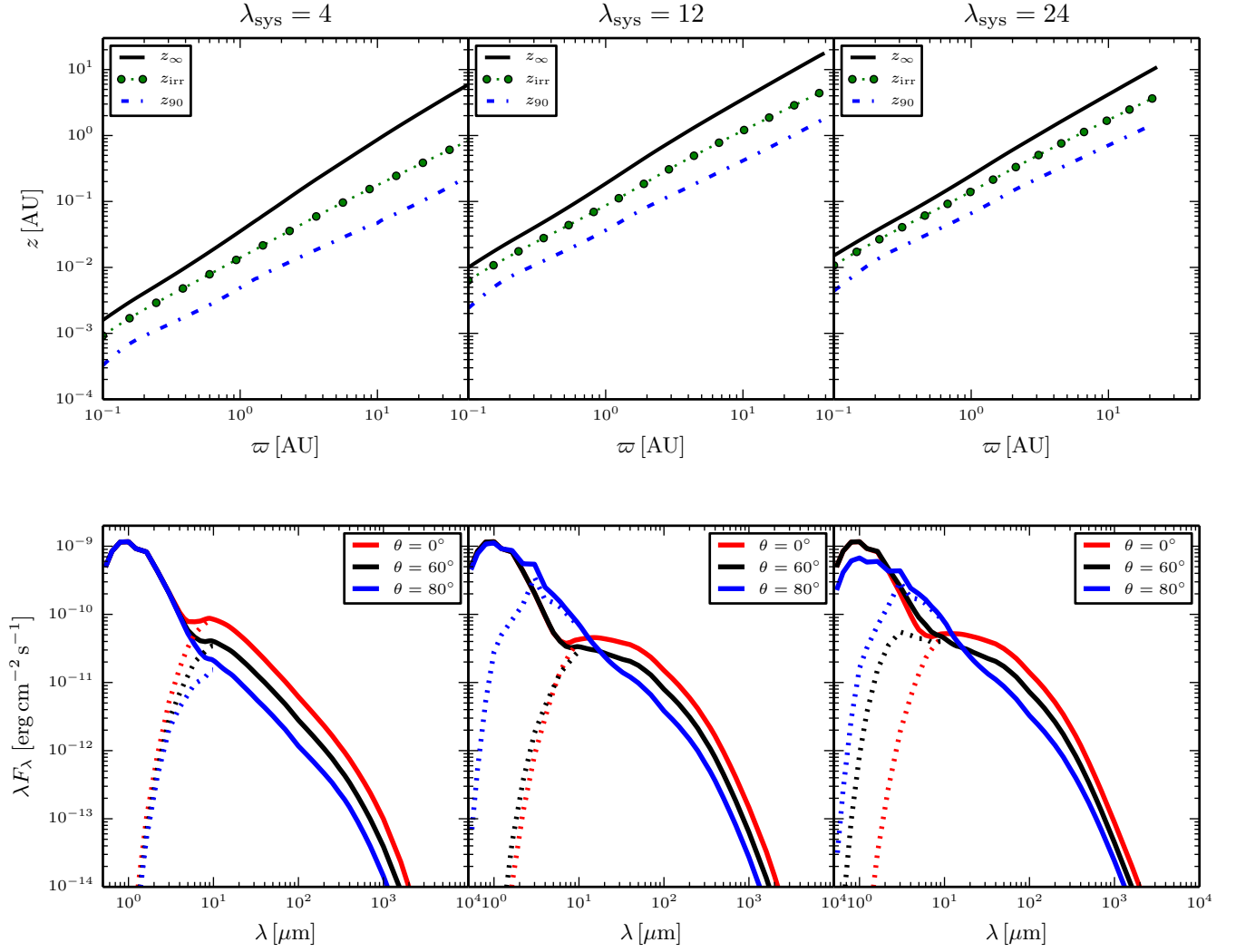


Figure 4. T Tauri disk model with a viscosity coefficient $D = 10^{-2.5}$ and different mass-to-flux ratios, $\lambda_{\text{sys}} = 4, 12, 24$, that label each column. The upper panels show the the different disk surfaces. The lower panels show the SED of the star plus disk system at different inclination angles. Same description as Figure 2.

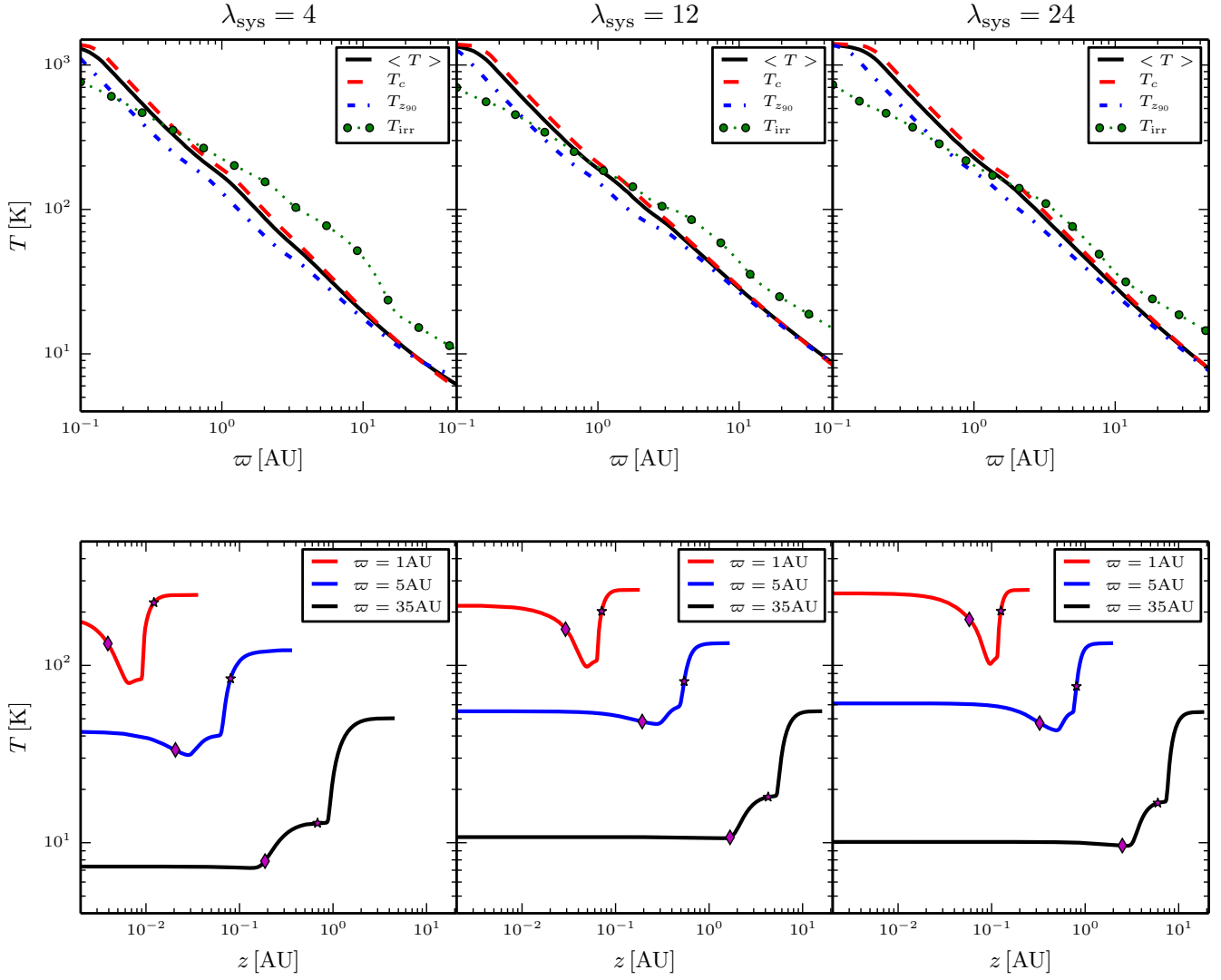


Figure 5. T Tauri disk models with viscosity coefficient $D = 0.01$ and different mass-to-flux ratios, $\lambda_{\text{sys}} = 4, 12, 24$, that label each column. The upper panels show the radial temperature profiles of the disks. The lower panels show vertical temperature structure at the radii indicated in the upper right boxes. Same description as Figure 1.

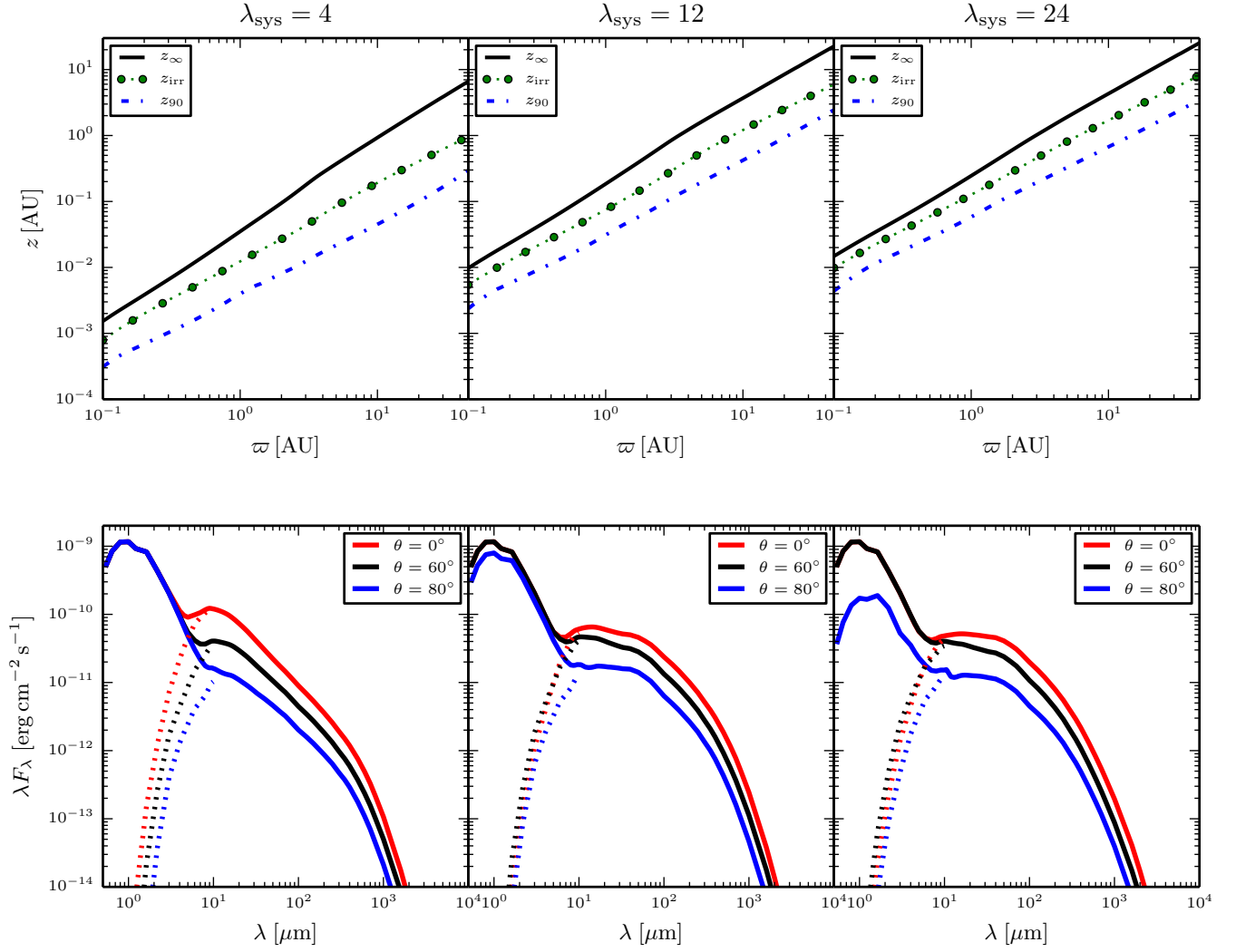


Figure 6. T Tauri disk model with a viscosity coefficient $D = 0.01$ and different mass-to-flux ratios, $\lambda_{\text{sys}} = 4, 12, 24$, that label each column. The upper panels show the the different disk surfaces. The lower panels show the SED of the star plus disk system at different inclination angles. Same description as Figure 2.

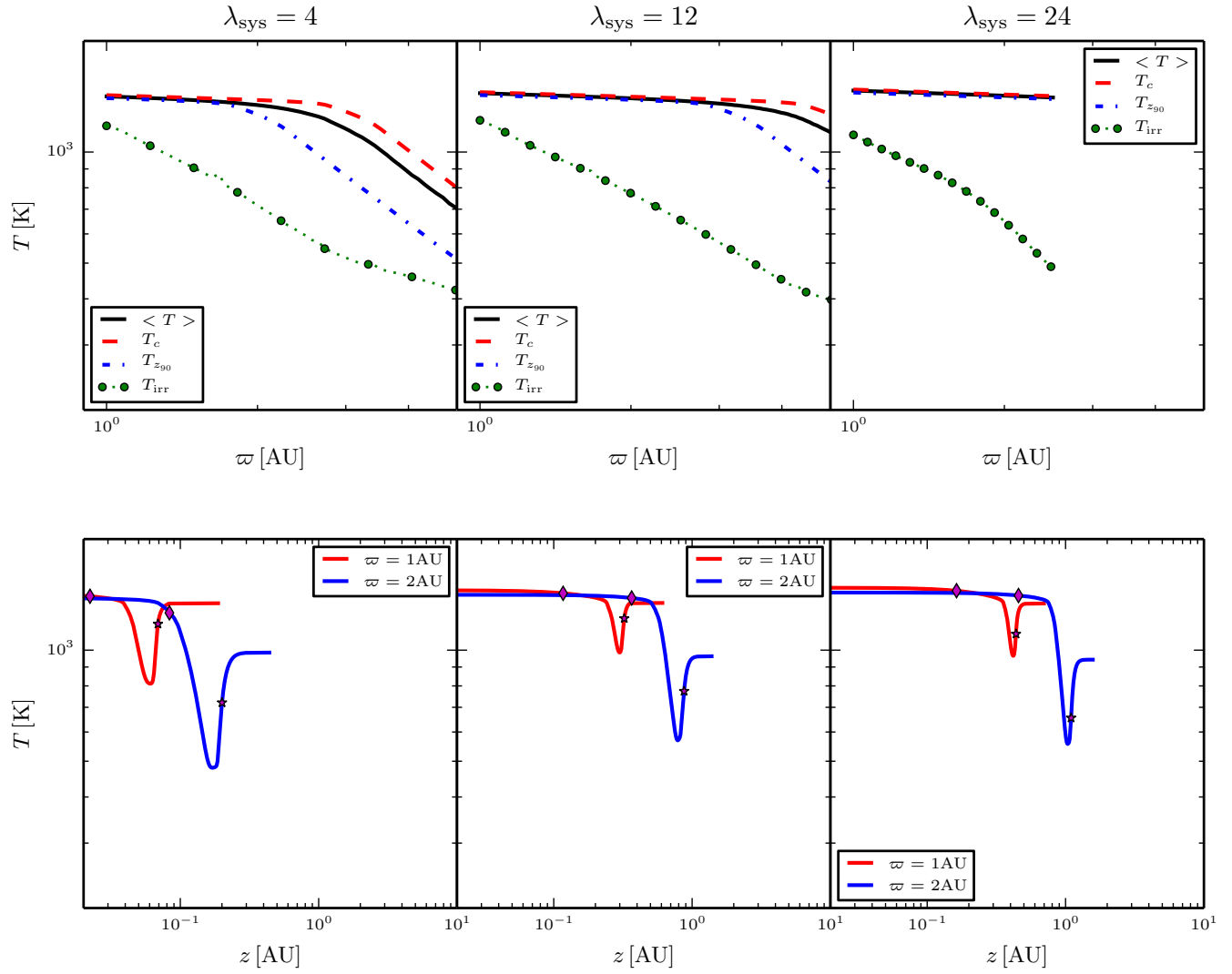


Figure 7. FU Ori disk models with different mass-to-flux ratios, $\lambda_{\text{sys}} = 4, 12, 24$, that label each column. The upper panels show the radial temperature profiles of the disks. The lower panels show vertical temperature structure at the radii indicated in the upper right boxes. Same description as Figure 1.

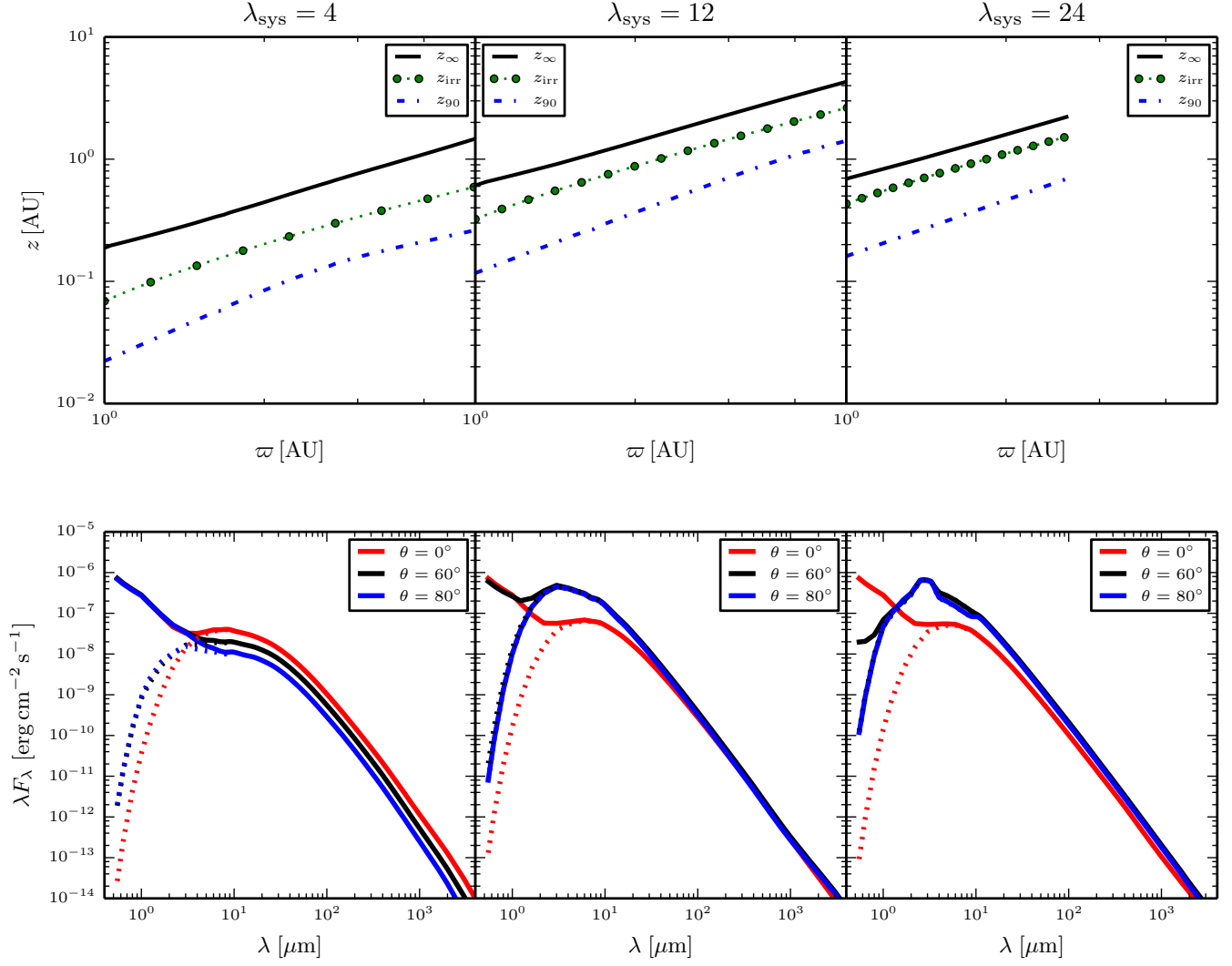


Figure 8. FU Ori disks with different mass-to-flux ratios, $\lambda_{\text{sys}} = 4, 12, 24$, that label each column. The upper panels show the different disk surfaces. The lower panels show the SED of the star plus disk system at different inclination angles. Same description as Figure 2.

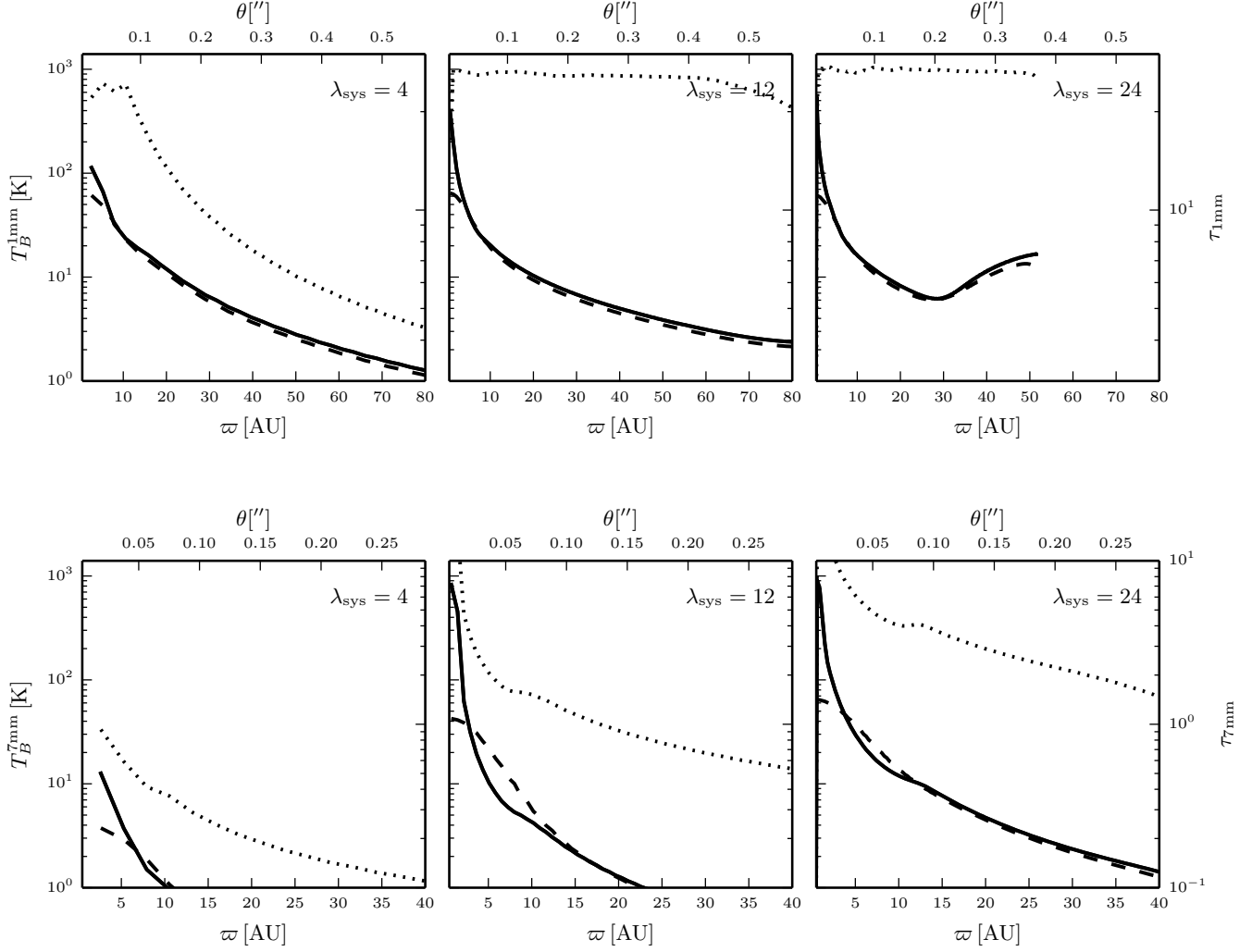


Figure 9. Averaged antenna temperature T_B and optical depth τ_λ profiles of the LMP disk models with different mass-to-flux ratios, $\lambda_{\text{sys}} = 4, 12, 24$, as a function of distance to the central star. The 1 mm and 7 mm profiles are shown in the upper and lower panels, respectively. The disk models have an inclination of $\theta = 60^\circ$. The solid lines in each panel correspond to the antenna temperature profiles. The dashed lines correspond to the antenna temperature profiles convolved with the ALMA beam at 1 mm, $\theta_{\text{ALMA}} = 0.034''$, and the VLA beam at 7 mm, $\theta_{7\text{mm}} = 0.043''$, respectively. The dotted lines correspond to the optical depth, the values are shown in the left axis in each panel. The upper axes gives the distance to the center in arcseconds, assuming a distance to the source of 140 pc.

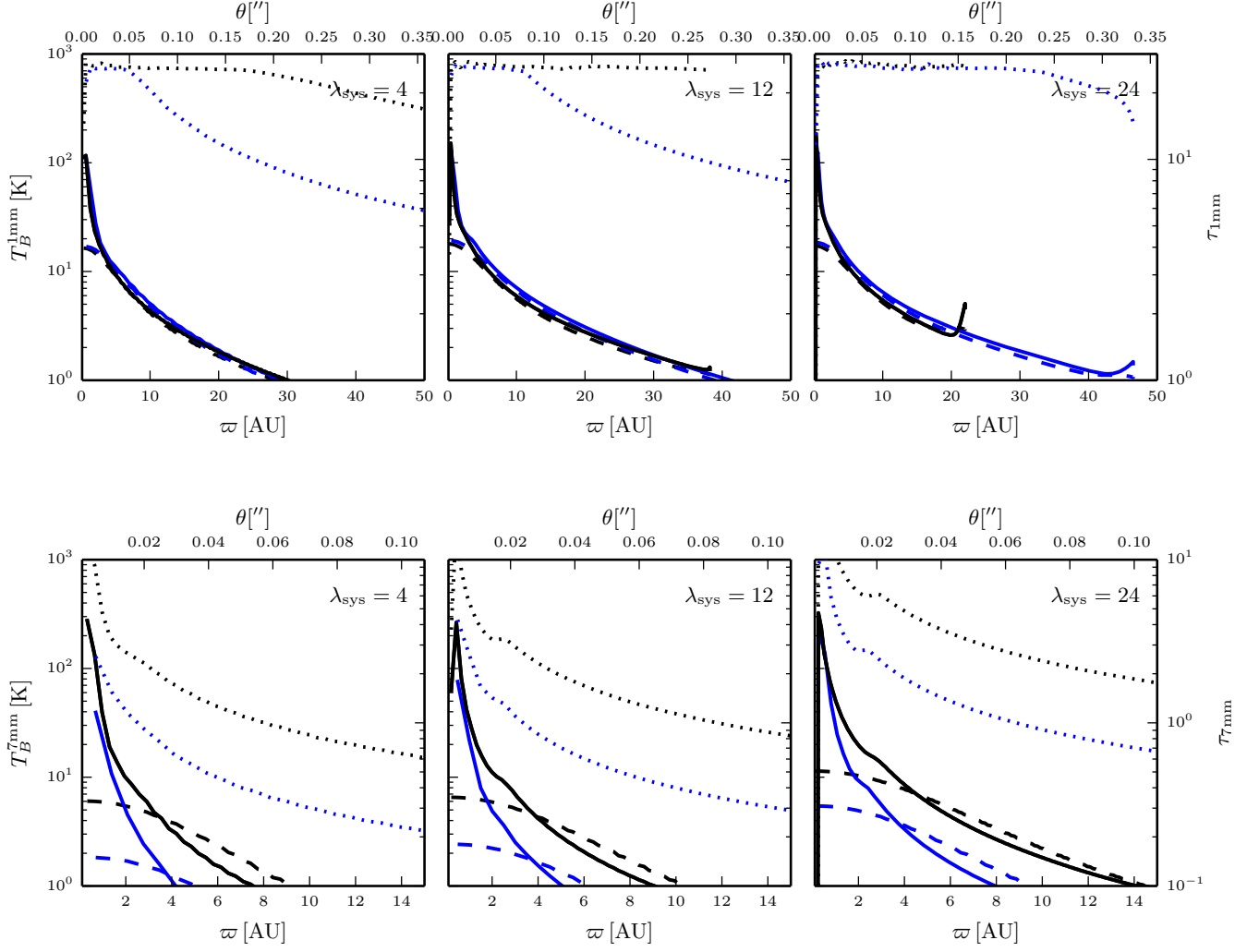


Figure 10. Antenna temperature T_B and optical depth τ_{λ} at 1 mm and 7 mm of T Tauri disks with different mass-to-flux ratios, $\lambda_{\text{sys}} = 4, 12, 24$, as a function of distance to the central star. The description of the panels and the lines is the same as in Figure 9. The black color lines correspond to models with a viscosity coefficient $D = 10^{-2.5}$, and the blue color lines correspond to a viscosity coefficient $D = 0.01$.

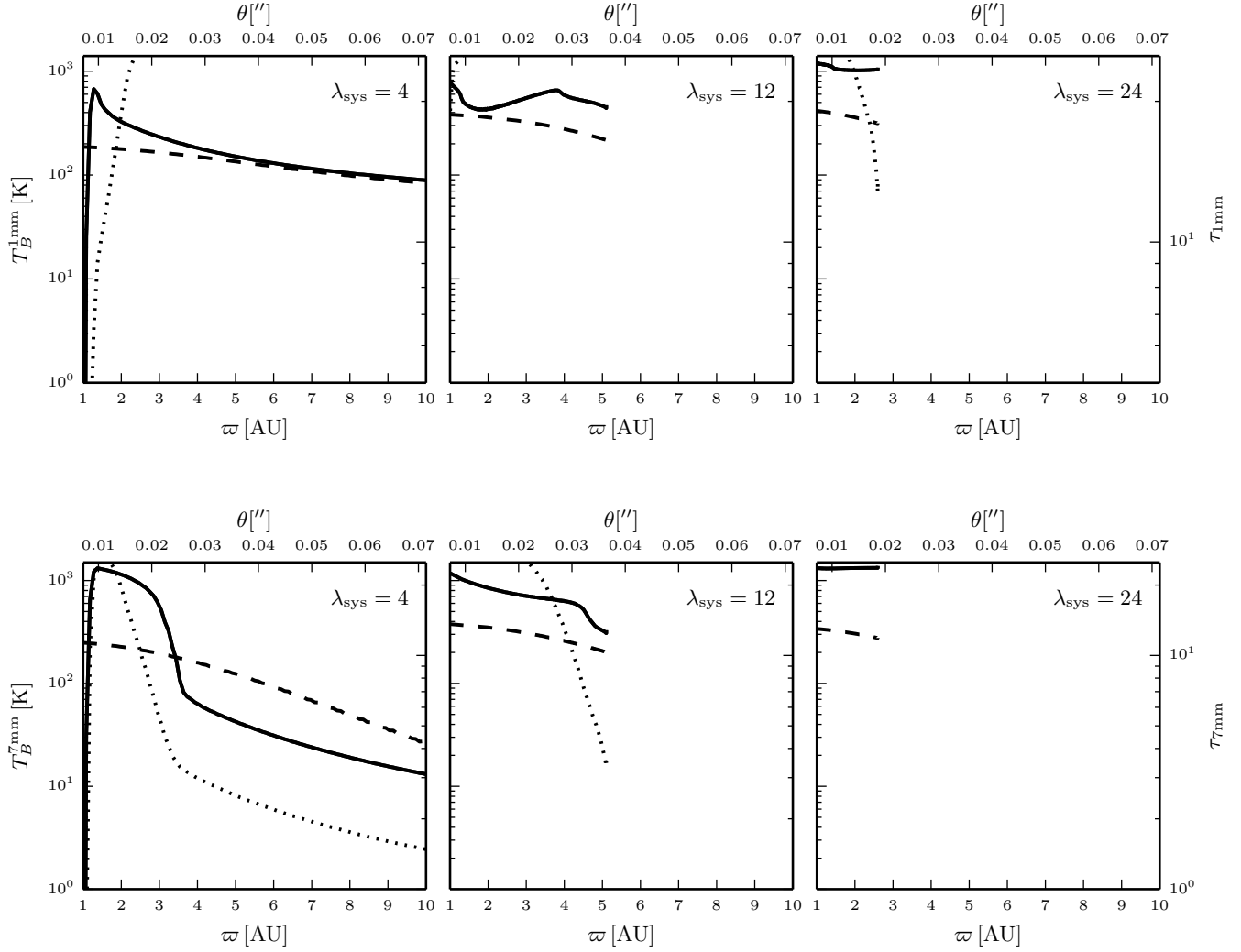


Figure 11. Antenna temperature T_B and optical depth τ_λ at 1 mm and 7 mm of FU Ori disks with different mass-to-flux ratios, $\lambda_{\text{sys}} = 4, 12, 24$, as a function of distance to the central star. The description of the panels and the lines is the same as in Figure 9. The upper middle panel and the lower right hand panel do not show the optical depth profile because, for numerical convenience, the integration of the optical depth ends at the value 25.

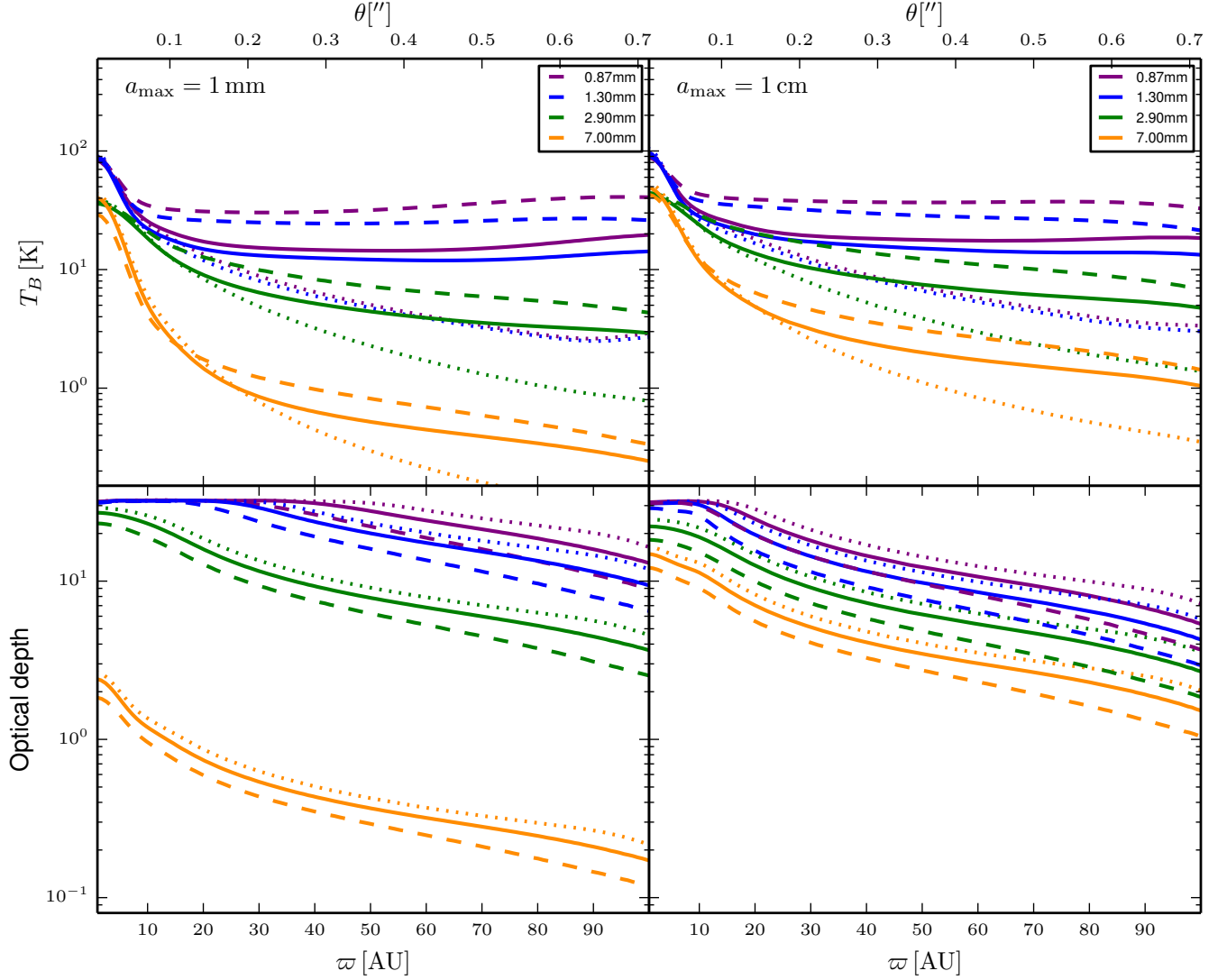


Figure 12. Antenna temperature T_B and optical depth τ_λ at 0.87, 1.3, 2.9, and 7 mm of LMP disks as a function of distance to the central star. The radial profiles have been convolved with the ALMA beams: $\theta_{0.87\text{ mm}} = 0.034''$, $\theta_{1.3\text{ mm}} = 0.029''$, $\theta_{2.9\text{ mm}} = 0.066''$, and the VLA beam at 7 mm, $\theta_{7\text{ mm}} = 0.043''$. The color code is shown in the boxes in the upper right corners. This color code is similar to the one used in Figure 3 of Carrasco-González et al. (2016) that plots the observed ALMA and VLA antenna temperature profiles of HL Tau. The disks have a mass-to-flux ratio $\lambda_{\text{sys}} = 24$. The disk parameters are shown in Table 4. The upper panels show T_B and the lower panels show τ_λ for each wavelength. The left panels correspond to models with a dust grain distribution with $a_{\text{max}} = 1$ mm: Model I (dotted lines) without envelope heating ($T_e = 0$ K); Model II (solid lines) with $T_e = 50$ K; Model III (dashed lines) with $T_e = 100$ K. The right panels correspond to models with $a_{\text{max}} = 1$ cm: Model IV (dotted lines) without envelope heating ($T_e = 0$ K); Model V (solid lines) with $T_e = 50$ K; Model VI (dashed lines) with $T_e = 100$ K.